
Article:
Issa, I., Ford, K.L. orcid.org/0000-0002-1080-6193, Rao, M. et al. (1 more author) (2016) The Enhancement of Radio Frequency Magnetic Field for a 1.5 Tesla Magnetic Resonance System Using a High Impedance Surface. IET Microwaves, Antennas and Propagation. ISSN 1751-8733

https://doi.org/10.1049/iet-map.2016.0088

The Enhancement of Radio Frequency Magnetic Field for a 1.5 Tesla Magnetic Resonance System Using a High Impedance Surface

Ismail Issa[1], Kenneth Lee Ford[2], Madhwesha Rao[3], James Wild[4]

[1]Department of Electronic and Electrical Engineering, The University of Sheffield, Sheffield, S1 3JD, UK
[2]Department of Electronic and Electrical Engineering, The University of Sheffield, Sheffield, S1 3JD, UK
[3]Department of Academic Radiology, The University of Sheffield, Sheffield, S10 2TN, UK.
[4]Department of Academic Radiology, The University of Sheffield, Sheffield, S10 2TN, UK.
[*]l.ford@sheffield.ac.uk

Abstract: This paper presents a novel design of a High Impedance Surface (HIS) to improve the magnetic field strength of a Radio Frequency (RF) coil at 63.8 MHz, suitable for 1.5T magnetic resonance imaging (MRI) systems. The HIS is miniaturized using distributed interdigital capacitors. A HIS with an electrically small unit cell ($\lambda/94$) and is positioned between a RF transmit-receive (TR) coil and an RF shield. The magnitude of the magnetic field from an RF coil when coupled to a dielectric phantom load (mimicking a biological sample) was estimated using numerical simulation (finite integral methods) and corroborated with measurements. Simulated median improvements in magnetic field inside a dielectric phantom range from approximately 18% to 32% depending on the area of the HIS.

1. Introduction

Magnetic Resonance Imaging (MRI) is a technology which yields tomographic information of the distribution of hydrogen atoms in a biological sample [1, 2]. The MRI technique is based on Nuclear Magnetic Resonance (NMR) phenomenon that excites the nuclear spin alignment in the presence of a static magnetic field and detects the subsequent Larmor precession of the nuclear spin magnetic moment by the process of Free Induction Decay (FID). In conventional MRI the protons within the water content of biological tissues are the nuclei of interest. MRI has been used for many diagnostic medical imaging applications in multiple organs in the human body, [3]. Spin excitation and subsequent signal detection of the FID is achieved with Radio Frequency (RF) coils resonating at the Larmor frequency of the relevant nucleus being imaged, which scales linearly with the applied static magnetic field strength. These coils are typically placed inside a Perfect Electrical Conductor (PEC) ground plane (the RF shield) in order to shield the resonators from other conducting objects inside the MRI system such as the gradient field. A typical RF coil will be proximal to the subjects anatomy in order to maximize the coupling to the sample. The signal-to-noise ratio (SNR) of the sampled signal is determined by the sensitivity of the RF coil to the biological sample, which is a function of the RF magnetic field. The Larmor precession in the biological sample not only induces RF current in the RF coil but also induces an out-of-phase RF current in the PEC shield which reduces the maximum available SNR, thus reducing the MRI

image quality, [4].

Previous research has shown that metamaterials, [5], can be used to improve the SNR of RF coils in MRI systems. A metamaterial is a periodic arrangement of resonant elements to achieve properties such as negative permeability and permittivity which are not observable otherwise. Previous studies have explored several techniques which include lattice of parallel and conducting thin wires [6], wave flux guides and lenses, specifically Swiss rolls, [7], and capacitively loaded metallic rings (CLRs) [8], which have a key advantage over other devices when they are designed as in a cubic lattice as they achieve 3D isotropy (homogeneity) which is essential for uniform H_1 RF field coverage over the biological sample, [9]. It was proposed in, [9], to use a magneto inductive (MI) lens to improve SNR of the images obtained by a RF surface coil operating at different Larmor frequencies. This study found that the SNR of the MR image could be increased by using a combination of a RF coil with a MI lens on a 3T MRI system, however, improvements at 0.5T and 1.5T were not as high. Recent research, [10], has investigated the use of a metasurface inside a dielectric medium with a biological sample showing an 2.7 fold increase in SNR. RF surface coils are usually placed at close proximity to the patient, whereas, metamaterial flux guides have also been used to couple the signal from the sample to an RF coil that is less proximal thus enabling interesting receiver possibilities for enhanced SNR e.g. by cryogenic cooling of the RF coil, [7]. Although the use of metamaterial lenses has advantages, the homogeneity of the delivered RF field is an area which could be improved through the use of High Impedance Surface (HIS) which can offer non-focused enhancements of magnetic fields.

The purpose of this study was to investigate the potential benefits of the use of HIS and to present a design methodology for improving the strength of the H_1 RF field inside a dielectric phantom (acting as human body or equivalent in an MRI scan). A Perfect Magnetic Conductor (PMC) has a reflection phase of 0°, whilst a PEC has a 180° reflection phase for a generally incident plane wave, [11]. The properties of a PMC can be produced using a HIS which is an Artificial Magnetic Conductor (AMC) that exhibits in-phase reflection properties over a specific frequency range, [12]. Previous studies, [13, 14], have reported the properties of HIS with RF coils on a 7T MRI system operating at 300MHz which used electrically small HIS unit cells of only 7.5% of free space wavelength. Using this method the H_1-field magnitude was improved by 47%. The challenge for successful implementation of HIS at lower RF frequencies of the order 60 MHz to 130 MHz which are the operating frequencies of a typical clinical MR scanner is the miniaturization of the HIS unit cells. Techniques for reducing the cell size dimensions of AMCs have been presented using multilayer structures, [15], lumped elements, [16, 17], and interdigital capacitance [18, 19]. This study aims to improve the magnetic field strength of the RF field of coils operational on a 1.5T MRI system at 63.8MHz. To accomplish this, an interdigital capacitance approach is used for the unit cell of the HIS. The efficacy of the approach is demonstrated with simulations and measurements of the magnetic field within a dielectric phantom for various design parameters of the proposed HIS.

2. MRI Concept and HIS Design

Fig.1a shows a schematic representation of a shielded (PEC) RF coil which is proximal to a dielectric phantom where the implementation is appropriate for a classic planar surface coil imaging approach. Fig. 1b shows the proposed system which includes a capacitive layer between the RF coil and PEC shield. The cross-sectional area (X_{HIS}^2) of the capacitive layer and PEC shield are equal and it is assumed that the thickness of the capacitive and PEC layers are electrically small.

The combination of the capacitive layer and the PEC shield forms a high impedance surface (HIS). The properties of the dielectric phantom were $\epsilon_r = 65$ and $\sigma = 0.4\ S/m$, [20], with dimensions x=14cm, y=33.5cm and z=23cm. The distance between the coil and phantom, s, was 5mm which is similar to practical MRI systems for safety reasons [21].

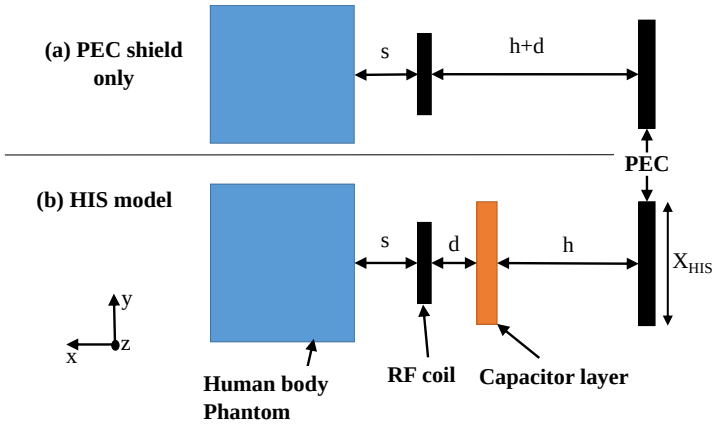

Fig. 1. *Cross-sectional view of the RF system (a) PEC shield only (b) HIS model.*

Fig.2 shows (a) the cross section of the HIS (Y_0 denotes the admittance of freespace), (b) a unit cell of the proposed capacitive layer which comprises of inter-digital metallic elements and (c) the equivalent circuit of the HIS. The PEC layer, spaced a distance, *h*, away from the capacitive layer, has an equivalent admittance that is inductive ($Y_{PEC} = -jcot(\beta h)$) where β is the freespace propagation constant. The capacitive surface acts as a shunt admittance such that the total input admittance is given by $Y_{in} = Y_{PEC} + Y_C$.

The inter-digital capacitive surface was adopted in order to maximize the capacitance density, [18], and provide an electrically small unit cell design. It was assumed that the capacitive layer has a 0.8mm thick FR4 substrate ($\epsilon_r = 4.3, tan\delta = 0.025$) and that it is placed 50mm away from the RF shield which acts as the ground plane for the HIS. This thickness is commensurate with the practical dimensions that might be found in MRI systems. In order to achieve a dual polarised HIS a second capacitive surface, labelled "back surface" in Fig. 2a, is on the reverse of the FR4 substrate, however, the back surface is rotated through 90° and as such the unit cell is rotationally symmetric. An illustration of the orientations of the digits is shown in Fig. 2b.

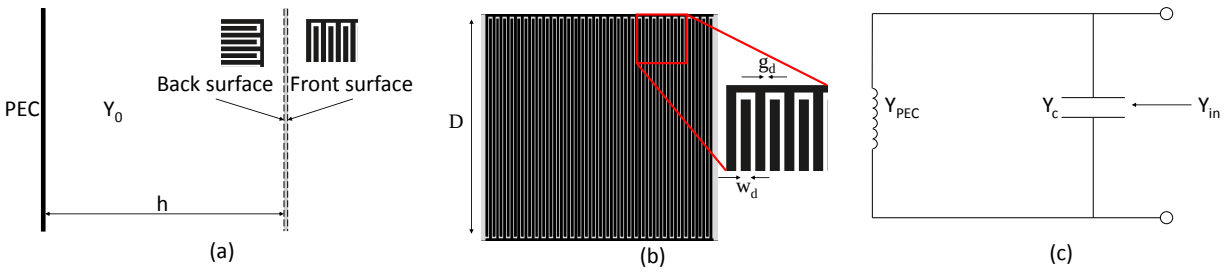

Fig. 2. *(a) Cross section of HIS, (b) front layer of capacitive surface and (c) equivalent circuit of HIS*

Initially the design of the HIS was carried out using approximations for interdigital capacitance, [22], using (1) where the units of capacitance are *pF*. When using the approximation equations it

was assumed that the second capacitive layer on the back surface was transparent.

$$C = \frac{\epsilon_{eff}(N-1)D}{18\pi}\frac{K(k)}{K'(k)} \tag{1}$$

where

$$\frac{K(k)}{K'(k)} = \begin{cases} \frac{1}{\pi} ln\left[\frac{2(1+\sqrt{k})}{1-\sqrt{k}}\right] & 0.707 \leq k \leq 1 \\ \frac{\pi}{ln\left[\frac{2(1+\sqrt{k'})}{1-\sqrt{k'}}\right]} & 0 \leq k \leq 0.707 \end{cases} \tag{2}$$

and

$$k = \tan^2\left(\frac{a\pi}{4b}\right), a = w_d/2, b = \frac{w_d + g_d}{2}, k' = \sqrt{1-k^2} \tag{3}$$

where K(k) is the complete elliptic integral of the first kind and its complement is K'(k), D is the digit length, N is the number of digits, $\epsilon_{eff} = \frac{\epsilon_r+1}{2}$, w_d is the width of the digits and g_d is the space between the digits. In the approximation the loss of the substrate is not included, however, this was included in later full field simulations. The reflection coefficient of the HIS can be calculated using (4). This approximation considerably simplifies the design process when compared to a full field analysis and optimization.

$$\rho = \frac{Y_0 - Y_{in}}{Y_0 + Y_{in}} \tag{4}$$

Fig. 3 shows the reflection phase for the proposed dual polarised HIS where D=48.5mm, with a 0.5mm gap between the end of the digits and the metallic horizontal strip. The number of digits, N=64, w_d= 0.5mm, g_d= 0.25mm, the unit cell inter element spacing is 1mm resulting in a unit cell periodicity of 50mm which is $\lambda/94$ at 63.8MHz. For comparison CST Microwave Studio frequency domain simulations were carried out using periodic Floquet mode boundary conditions to approximate an infinite HIS and the CST simulations included the substrate and copper losses and both capacitive layers were incorporated into the simulation. It can be seen that there is good agreement between the approximate equivalent circuit model and the CST simulations. Fig. 4 shows a photograph of the manufactured HIS to be used in later measurements.

3. RF Coil Design and Characterisation

Fig. 5 shows an schematic of a single loop RF transmit/receive surface coil which is realized with lumped capacitance to tune the resonance of the coil to the appropriate Larmor frequency, specifically 63.8MHz for a 1.5T MRI system. The coil has an equivalent circuit of a series inductance and capacitance where the inductance (nH) can be estimated using (5), [23] where the dimensions are in mm. The required capacitance to tune the resonant frequency to 63.8MHz can be calculated accordingly. Fig. 5 also shows the manufactured coil including lumped components and balun.

$$\begin{aligned} L = \; & 0.921\left[(S_1+S_2)\log\left(\tfrac{2S_1S_2}{b+c}\right) - S_1\log(S_1+g) - S_2\log(S_2+g)\right] \\ & +0.4\left[2g - \tfrac{S_1+S_2}{2} + 0.447(b+c)\right] \end{aligned} \tag{5}$$

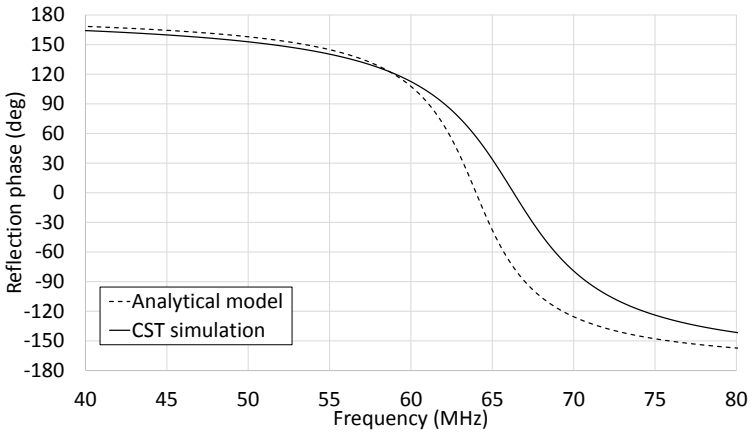

Fig. 3. *Reflection phase of proposed dual polarised HIS*

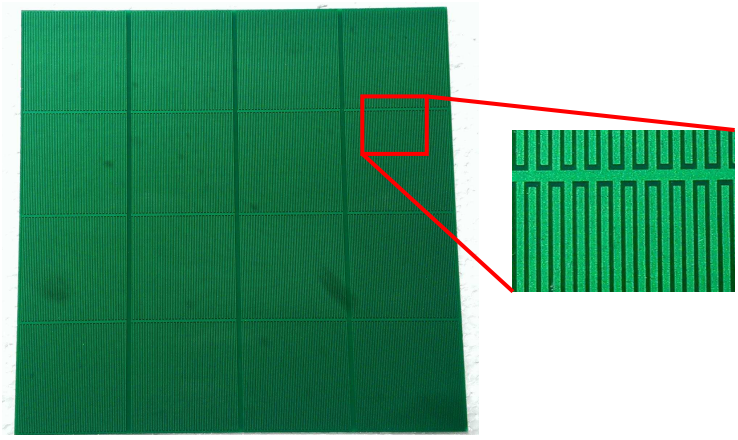

Fig. 4. *Front layer of manufactured dual polarised capacitive surface.*

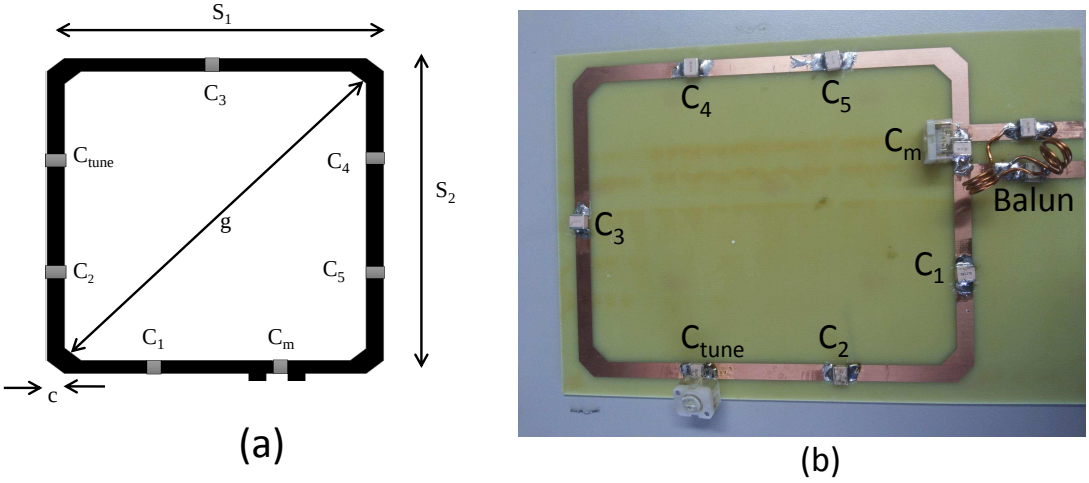

Fig. 5. *(a) Schematic and (b) manufacture RF coil*

The dimensions of the coil are shown in Fig. 5 with a coil metal thickness, b. The designed coil has dimensions, S_1=120mm, S_2=150 mm, b=32μm, g=192 mm and c=6mm with a 1.6mm thick FR4 substrate. The coil material was assumed to be copper with no surface roughness and a conductivity of 5.8*10^7 S/m. The resulting equivalent inductance and total capacitance are (L=414nH) and (C_t=15pF) respectively. The coil was simulated using CST Microwave Studio incorporating seven capacitors (C_1 to C_5, C_m and C_{tune} as illustrated in Fig. 5). The fixed capacitors, C_1 to C_5, are 100pF and C_m and C_{tune} are variable capacitors (7-100) pF. C_m is used to match the coil in the presence of the dielectric phantom and HIS and C_{tune} is used to tune the resonant frequency of the RF coil. The RF power was fed to the coil through a balun circuit which is connected either side of C_m.

Fig. 6 shows the simulated and measured input match (S11) when the coil is spaced 5mm away from a dielectric phantom consisting of 5L distilled water and 200g Sodium Chloride which was placed inside a plastic container with the same dimensions as used in Fig. 1. In the experimental system the manufactured coil was connected to an Agilent E5071B Vector Network Analyser (VNA) and the resonant frequency was tuned to 63.8MHz using the variable capacitor, C_{tune}, in the presence of the HIS and dielectric phantom and the magnitude of S11 was controlled using C_m. Also presented is the S11 when the HIS is removed which has the effect of shifting the measured resonance from 63.8MHz to 64.6MHz. It was possible to tune the resonant frequency back to 63.8MHz with the use of C_{tune} for later field measurements. The difference between measurement and simulation is due to tolerances in the lumped capacitor values, the coil inductance approximation and material property assumptions.

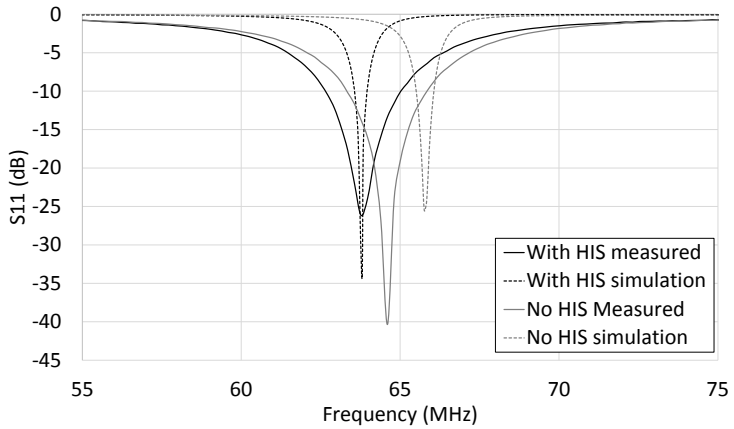

Fig. 6. *Simulation and measurement of input match of RF coil*

4. Simulated results with a dielectric phantom

In order to reduce simulation complexity for the scenario shown in Fig. 1 the capacitive layer was implemented as an effective surface impedance model which has been previously shown to be an effective approach [8, 14]. The surface impedance was determined using full field simulations of the dual polarised unit cell of the capacitive layer using CST. The impedance is complex and includes the losses due to the FR4 substrate and copper losses. Fig. 7 shows the CST simulation geometry including the dielectric phantom, RF coil, capacitive layer and PEC shield.

CST simulations were carried out for both models in Fig. 1 where the magnitude of the magnetic

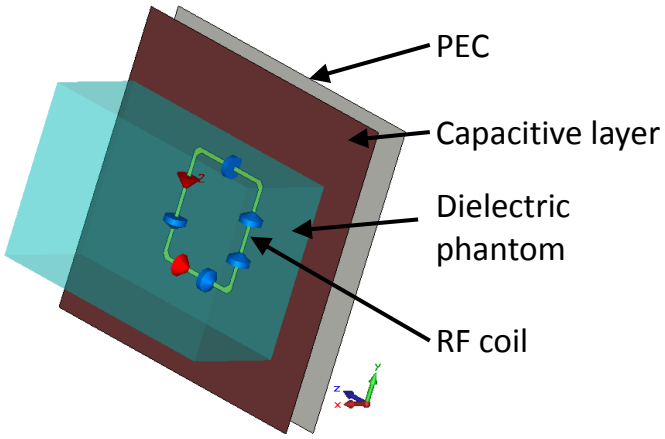

Fig. 7. *CST simulation geometry.*

field inside the dielectric phantom was monitored along the x-axis (y=z=0) and y-axis (x=140mm, z=0) assuming s=d=5mm and the RF coil was fed by a 1W, 50Ω source. For a fair comparison the magnetic field was normalised to the square root of the accepted power in the phantom.

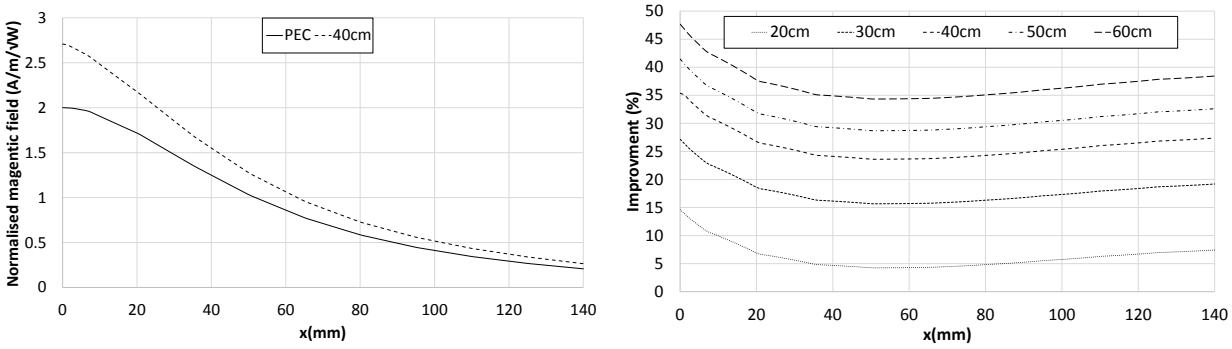

Fig. 8. *Normalised magnitude of simulated magnetic field (left) and improvement in normalised magnetic field (right), along x axis for varying HIS area.*

Of particular interest is the impact of the cross-sectional area of the HIS where in practice there would be a trade off between magnetic field enhancement and available space in an MRI system which typically have internal diameters of approximately 60cm. Fig. 8 (left) shows the normalised magnetic field when X_{HIS} =40cm and the PEC only case, along the x-axis. It can be seen that there is an improvement over the full range of the x-axis. A more in-depth analysis is shown in Fig. 8 (right) which shows the improvement in magnetic field compared to a PEC shield of the same cross section. As X_{HIS} increases the improvement in magnetic field increases. Similar results are observed along the y-axis, shown in Fig. 9.

Further analysis of the magnetic field throughout the volume of the dielectric phantom, in the form a cumulative density function of the magnetic field, is shown in Fig. 10 and the median improvement in magnetic field inside the dielectric phantom, compared to the PEC only case, versus cross-sectional dimension is shown in Table 1. Fig.11 shows the magnitude of the magnetic field in *xy* plane and further illustrates the improvement which can be achieved.

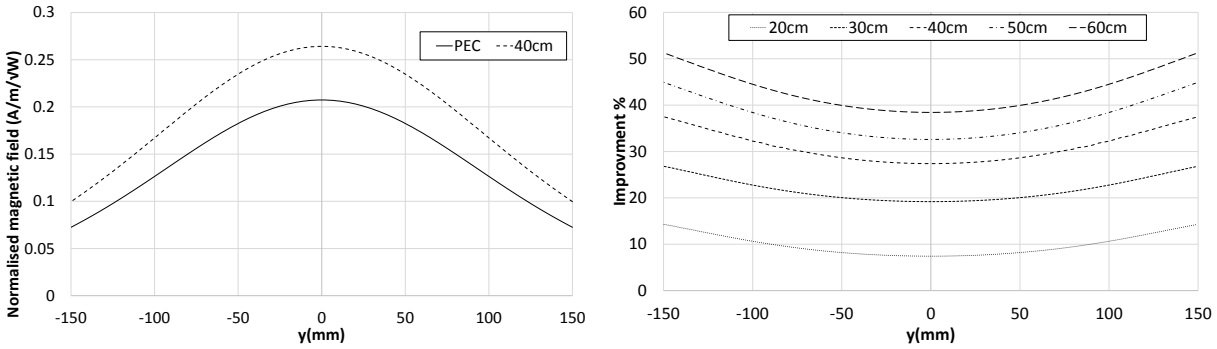

Fig. 9. *Normalised magnitude of simulated magnetic field (left) and improvement in normalised magnetic field (right), along y axis for varying HIS area.*

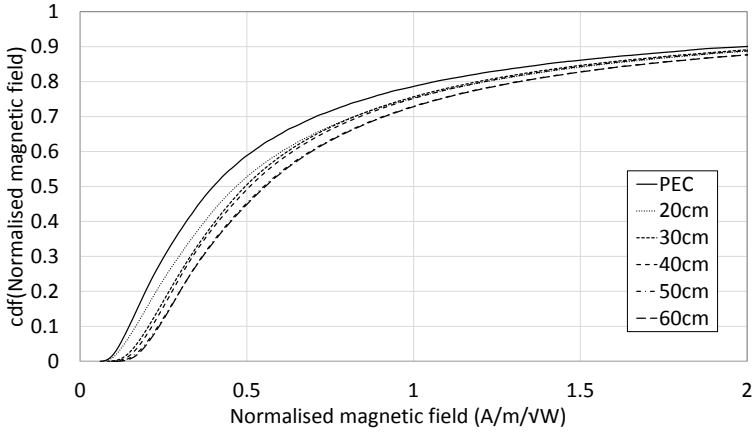

Fig. 10. *Cumulative density function of normalised magnetic field within the dielectric phantom*

Table 1 Simulated median improvement in RF magnetic field (%) versus X_{HIS}

X_{HIS}	20cm	30cm	40cm	50cm	60cm
% improvement	18	22	24	31	32

5. Experimental Results with a Dielectric Phantom

To demonstrate the concept a capacitive layer was manufactured for X_{HIS}=40cm using a chemically etched $32\mu m$ copper layer on a FR4 substrate comprising of four (20cm x 20cm) individual surfaces. Fig. 12 shows a photograph of the experimental set-up.

A 5cm diameter magnetic flux probe which was built in-house using semi-rigid coaxial cable was manufactured and the transmission coefficient (S21) between the RF coil and flux probe was measured such that comparisons between the models in Fig. 1 could be carried out. As the flux probe is an electrically small loop, where the resonant frequency of the loop was measured to be 2.2GHz, it was assumed that the probe will have negligible effect on the measurements and the comparisons against simulations is valid. Fig. 13 (left) shows the normalised measured S21 along the x-axis ($y = z = 0$) and Fig. 13 (right) shows the normalised S21 along the y-axis ($x = 140mm, z = 0$). The S21 was normalised to the maximum of the PEC case for ease of comparison. The improvement in magnetic field (x=5mm and x=140mm, y=z=0) is 27% and 23%

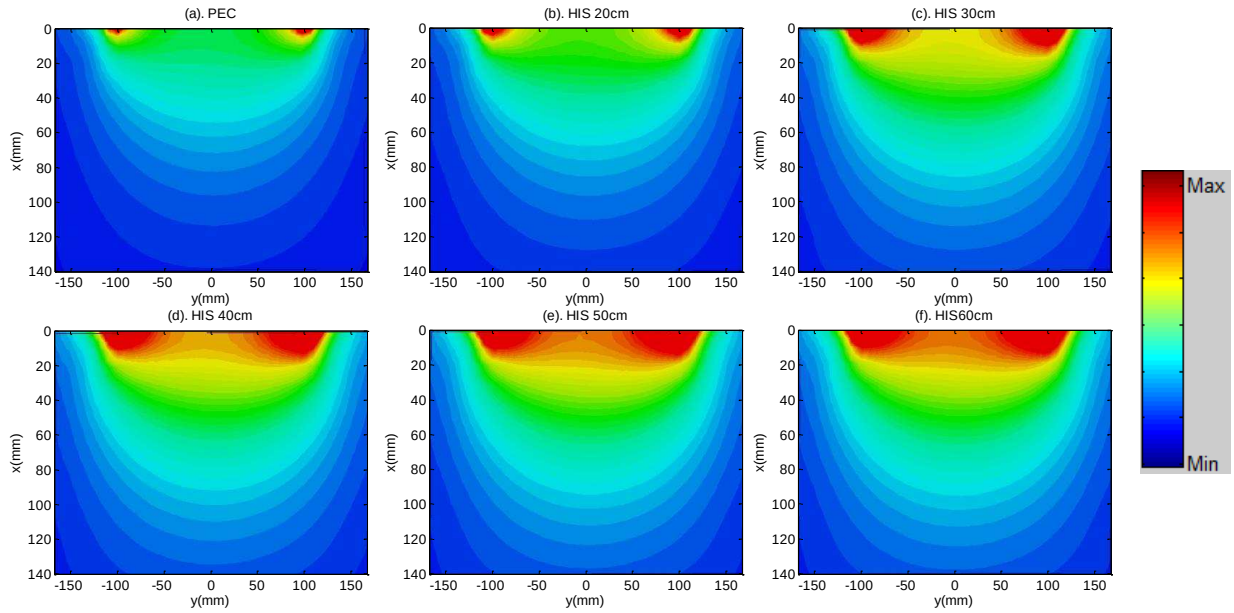

Fig. 11. *Simulated magnitude of magnetic field inside dielectric phantom*

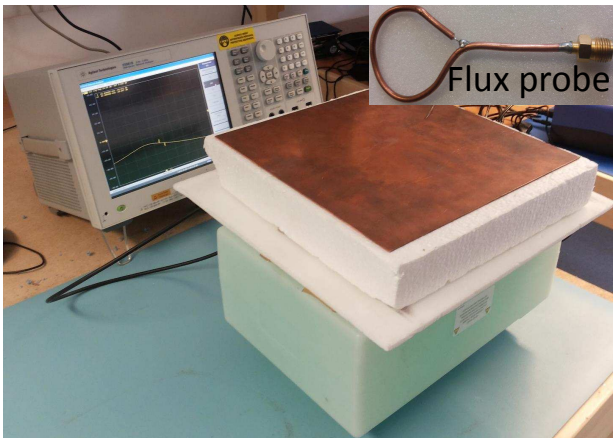

Fig. 12. *Experimental set-up*

respectively which is lower than the simulations due to tolerances in fabrication and uncertainties in material losses, however, the overall trends are similar.

6. Conclusion

In this paper, numerical simulations and experimental results show that a miniaturized HIS can be used for improving the magnetic field for MRI applications where the proposed HIS has a unit cell size of $\lambda/94$ at 63.8MHz. Moreover, our work has investigated the normalised H_1 field provided by an RF coil with a HIS and homogeneous dielectric phantom for a range of HIS cross-sectional area, showing that the improvement in magnetic field increases with HIS area. The concept has been demonstrated through measurements. Future work will focus on demonstrating the approach

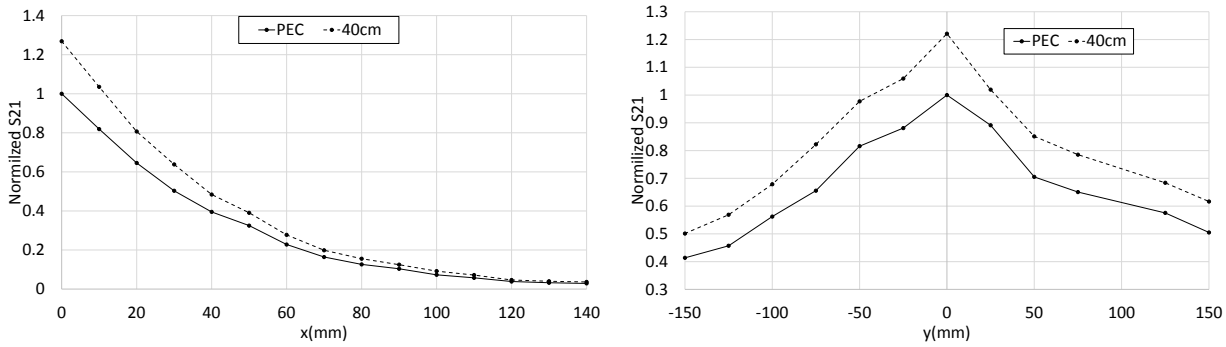

Fig. 13. *Normalised magnitude of measured S21 along x axis (left) and y axis (right)*

in a MRI scanner, extending the approach to a cylindrical MRI geometry, using RF coil arrays and multi-nuclear MRI applications.

7. References

[1] M. Brown and R. Semelka, *MRI: Basic Principles and Applications*. Wiley, 2003.

[2] J. Vaughan and J. Griffiths, *RF Coils for MRI*. Wiley, 2012.

[3] K. Ugurbil, "Magnetic resonance imaging at ultrahigh fields," *IEEE Transactions on Biomedical Engineering*, vol. 61, no. 5, pp. 1364–1379, 2014.

[4] J. M. Jin, "Electromagnetics in magnetic resonance image," *IEEE Antennas and Propagation Magazine*, vol. 40, no. 6, pp. 7–22, 1998.

[5] R. Marqués, F. Martín, and M. Sorolla, *Metamaterials with Negative Parameters: Theory, Design and Microwave Applications*. Wiley, 2011.

[6] P. A. Belov and M. G. Silveirinha, "Resolution of sub-wavelength transmission devices formed by a wire medium," *Physical Review E*, vol. 73, no. 5, pp. 1–10, 2006.

[7] M. Wiltshire, J. Pendry, I. Young, and D. Larkman, "Microstructured magnetic material for RF flux guides in magnetic resonance imaging," *Applied Physics Letters*, vol. 291, pp. 849–851, 2001.

[8] M. Freire, R. Maeques, and L. Jelink, "Experimental demonstration of permeability= -1 metamaterial lens for magnetic resonance imaging," *Applied Physics Letter*, vol. 93, 2008.

[9] J. M. Algarin, M. Freire, and F. Breuer, "Metamaterial magnetoinductive lens performance as a function of field strength," *Journal of Magnetic Resonance*, vol. 247, pp. 9–14, 2014.

[10] A. P. Slobozhanyuk, A. N. Poddubny, A. J. E. Raaijmakers, C. A. T. van den Berg, A. V. Kozachenko, I. A. Dubrovina, I. V. Melchakova, Y. S. Kivshar, and P. A. Belov, "Enhancement of magnetic resonance imaging with metasurfaces," *Advanced Materials*, vol. 28, no. 9, pp. 1832–1838, 2016.

[11] N. Engheta and R. Ziolkowski, *Metamaterials: Physics and Engineering Explorations*. Wiley, 2006.

[12] D. Sievenpiper, Z. Lijun, R. F. J. Broas, N. G. Alexopolous, and E. Yablonovitch, "High-impedance electromagnetic surfaces with a forbidden frequency band," *IEEE Transactions on Microwave Theory and Techniques*, vol. 47, no. 11, pp. 2059–2074, 1999.

[13] G. Saleh, K. Solbach, and A. Rennings, "EBG structure to improve the B1 efficiency of stripline coil for 7 Tesla MRI," in *6th European Conference on Antennas and Propagation (EUCAP)*, pp. 1399–1401, 2012.

[14] Z. Chen, K. Solbach, D. Erni, and A. Rennings, "Electromagnetic field analysis of a dipole coil element with surface impedance characterized shielding plate for 7-T MRI," *IEEE Transactions on Microwave Theory and Techniques*, vol. 64, pp. 972–981, March 2016.

[15] R. Kuse, T. Hori, M. Fujimoto, T. Seki, K. Sato, and I. Oshima, "Equivalent circuit analysis for double layer patch type AMC in consideration of mutual coupling between layers," in *2013 Asia-Pacific Microwave Conference Proceedings (APMC)*, pp. 591–593, 2013.

[16] H. Liu, K. L. Ford, and R. J. Langley, "Miniaturised artificial magnetic conductor design using lumped reactive components," *Electronics Letters*, vol. 45, no. 6, pp. 294–295, 2009.

[17] R. Saad and K. L. Ford, "Miniaturised dual-band artificial magnetic conductor with reduced mutual coupling," *Electronics Letters*, vol. 48, no. 8, pp. 425–426, 2012.

[18] R. Saad and K. L. Ford, "A miniaturised dual band artificial magnetic conductor using interdigital capacitance," in *Antennas and Propagation (EuCAP), 2014 8th European Conference on*, pp. 25–26, 2014.

[19] G. D. Alley, "Interdigital capacitors and their application to lumped-element microwave integrated circuits," *IEEE Transactions on Microwave Theory and Techniques*, vol. 18, no. 12, pp. 1028–1033, 1970.

[20] K. Foster and H. Schwan, "Dielectric properties of tissues and biological material," *Critical Reviews in Biomedical Engineering*, vol. 17, pp. 25–104, 1989.

[21] N. Farber, J. McNeely, and D. Rosner, "Skin burn associated with pulse oximetry during perioperative photodynamic therapy," *The Journal of the American Society of Anesthesiologists*, vol. 84, pp. 983–985, 1996.

[22] I. Bahl, *Lumped Elements for RF and Microwave Circuits*. Artech House, 2003.

[23] F. E. Terman, *Radio engineers' handbook*. New York; London: McGraw-Hill Book Co., 1943.